PAPER

Flexible, conductive, porous, fibrillar polymer–gold nanocomposites with enhanced electromagnetic interference shielding and mechanical properties†

Jun Li,[a] Hu Liu,[b] Jiang Guo,[b] Zhen Hu,[a] Zhijiang Wang,[a] Bin Wang,[c] Li Liu,[a] Yudong Huang*[a] and Zhanhu Guo*[b]

Porous polymer nanocomposites with a density of only <0.26 g cm^{-3} and robust flexibility have been prepared by ionic self-assembly of gold nanoparticles (NPs) on the charged polymer skeleton made of poly(pyridobisimidazole)-grafted-poly(dimethyl diallyl ammonium chloride) (PIPD-*g*-PDDA) composite nanofibers. Toward electromagnetic interference (EMI) shielding, a shielding effectiveness of over −64.9 dB in the frequency range of 250 MHz–1.5 GHz was demonstrated in the as-obtained nanocomposites with a thickness of only 20 μm. The equivalent gold thickness of these films was 10–50 times thinner than the skin depth of 6–12 μm for the bulk gold in the same frequency range. The electrical conductivity of these composites was around 15 890 S cm^{-1} with the volume fraction of gold nanoparticles at 40.5%. The added nanoparticles enhanced the tensile strength by 12.4% as compared to the pure polymer films. No obvious degradation in electrical conductivity was observed even after repeatedly bending 1000 times with a bending radius of 1 cm. The shielding mechanism was disclosed by comparatively analyzing the reflection from the material surface (SE$_R$), the absorption of electromagnetic energy (SE$_A$), and the multiple internal reflection of electromagnetic radiation (SE$_M$).

1. Introduction

Modern electronics with highly integrated circuits often generate severe electromagnetic radiation waves, which can cause interference and thus malfunctioning of highly sensitive precision electronic equipment. Thus, effective protection from electromagnetic radiation is needed. The shielding of electromagnetic interference (EMI) can be achieved by either absorption or reflection, which can protect people from electromagnetic radiation and transport the electromagnetic signals away from the desired electronics. Great efforts have been made to develop high-performance EMI shielding materials.[1–7] Although absorption can permanently annihilate the microwave propagation, it normally generates heat from eddy current loss and can cause the degradation of the shielding performance. Reflection can

overcome the interference with much less heat generation, and can be used for the normal operation of electronics.

Besides high EMI shielding performance, light weight and flexibility are two important additional parameters considered for practical EMI shielding, especially in the areas of aircrafts, aerospace and flexible electronics such as portable electronics and wearable devices.[8] In the preparation of conductive, lightweight and flexible EMI shielding materials, the common strategy involves the design of robust and flexible polymer skeletons, followed by mixing, coating and/or depositing EMI shielding components.[8–15] In such a design, various structures including polymeric foams,[9,11,16,17] membranes[18] and porous networks[19] have been reported. The most popular design is mainly focused on the preparation of polymeric foams or networks, where electrically conductive fillers, such as Fe,[20–22] Ag,[12] Ni,[9] carbon fibers,[23] carbon nanotubes (CNTs)[24,25] and graphene,[26,27] are embedded in the polymer matrix. However, these conductive fillers are often randomly distributed inside the polymer matrix and surrounded by the electrical insulating polymer chains that are detrimental to the electrical conductivity. The primary reason is that the electrical conductivity strongly relies on the electron percolation of the separated conductive fillers. As a result, a high loading and well-defined dispersion of these fillers are usually required to form an electrically conductive interconnected

[a] *School of Chemical Engineering and Technology, State Key Laboratory of Urban Water Resource and Environment, Harbin Institute of Technology, Harbin 150001, China. E-mail: huangyd@hit.edu.cn*

[b] *Integrated Composites Laboratory (ICL), Department of Chemical and Biomolecular Engineering, University of Tennessee, Knoxville, TN 37996, USA. E-mail: zguo10@utk.edu*

[c] *Engineered Multifunctional Composites (EMC) Nanotech, Knoxville, TN 37934, USA*

† Electronic supplementary information (ESI) available. See DOI: 10.1039/c6tc04780g

This journal is © The Royal Society of Chemistry 2017

J. Mater. Chem. C, 2017, 5, 1095–1105 | 1095

network in the insulating polymer matrix. Hence, the required high electrical conductivity of these materials can be achieved to realize high EMI shielding effectiveness. In addition, thick samples are also necessary for these composites to shield EMI effectively. For example, graphene/polymethylmethacrylate (PMMA) composite foams showed a specific EMI shielding effectiveness of 17 dB cm^3 g^{-1} with a thickness of more than 2 mm.[13] However, these foam structures suffered from poor electrical conductivity because of low quality and/or high inter-sheet junction contact resistance of the fillers.

The simple blending of electrically conductive fillers in most intrinsic insulating polymeric matrices could dramatically suppress the electrical conductivity of their final composites. EMI shielding performance was limited even though lightweight robust polymer composites could be produced. As a consequence, the corresponding skin depth toward attenuating electromagnetic waves would be considerably enlarged.[24,28–30] In this situation, a thicker structure would be needed to reach the same shielding performance with similar materials showing a smaller skin depth. For example, Chen et al. used a template-directed CVD method to fabricate conductive graphene foams with a 3D interconnected network structure, exhibiting lightweight and high EMI shielding performance.[26] However, this porous graphene foam was not flexible enough and the electrical conductivity was also low compared with metals. Highly conductive network nanostructures decorated on a porous flexible polymer skeleton are promising for EMI shielding and have rarely been reported.

Herein, we report flexible porous polymer nanocomposites with a highly electrically conductive 3-D gold network on the polymer skeleton prepared by ionic self-assembly of gold nanoparticles (NPs) on the charged polymer skeleton made of poly(pyridobisimidazole)-grafted-poly(dimethyl diallyl ammonium chloride) (PIPD-g-PDDA) composite nanofibers. The composite nanofibers were synthesized through grafting poly(dimethyl diallyl ammonium chloride) (PDDA) on the surface of poly(pyrido-bisimidazole) (PIPD) nanofibers. The morphology of the nanocomposites was studied using scanning electron microscopy (SEM) and the particles were observed by atomic force microscopy (AFM). The thermal stability of these nanocomposites was evaluated. The mechanical properties were studied by the tensile test and the cyclic durability test. The electrical conductivity of the nanocomposites with different gold coatings was measured. Both real and imaginary permittivities were measured as a function of frequency for the nanocomposites with different coatings. The EMI shielding performance of these obtained composites was studied. The shielding mechanisms were revealed by comparatively studying the reflection from the material surface (SE$_R$), the absorption of electromagnetic energy (SE$_A$), and multiple internal reflections of electromagnetic radiation (SE$_M$).

2. Experiments

2.1 Sample preparation

The synthesis of porous PIPD-g-PDDA/Au composites is illustrated in Scheme 1. The PIPD nanofibers were chosen to build

interconnected 3D scaffolds as templates for the self-assembly of gold nanoparticles because of their high physicochemical performances including a strength of 4.5 GPa, a modulus of 400 GPa, thermal stability at higher than 480 °C, and excellent chemical resistance.[31] PIPD has many polar side groups –OH and skeleton groups –NH–, which make the macromolecular interaction very strong. The intermolecular hydrogen bonding network can be formed in the fiber form.[32] However, like most organic fibers, PIPD fibers show a fibrillar structure under shearing and compressive loads,[33] especially for the as-spun PIPD fibers which contain a lot of residual polyphosphonic acid solution. Meanwhile, the hydrogen bonding network in the as-spun PIPD fibers is not well-defined. In dimethyl sulfoxide (DMSO), the as-spun PIPD fibers without any treatment were found capable of being swelled easily at 95 °C under strong ultra-sonication and shearing, and were then stripped layer by layer. The PIPD nanofibers were obtained using this strategy and the morphology changes are shown as Fig. S1 (ESI†). Different from the reported Kevlar nanofibers,[34–36] no potassium hydrate was used and fewer PIPD macromolecules were degraded into small molecules, thus the nanofiber yield could reach ~97%. The PIPD nanofibers with different diameters were obtained by changing the stripping time, and the porous membranes were made by filtration of PIPD/DMSO solution. Similar to the reported results,[37–39] the specific surface area of the porous film increases sharply with decreasing the diameter, and the mass transport of water in the membrane decreases greatly with decreasing the nanofiber diameter.

Considering the specific surface area and mass transport necessary for further decorating gold nanoparticles, the PIPD nanofibers with an average diameter of 250 nm were chosen as the 3D skeleton in this study. To generate an ionic self-assembly of gold nanoparticles on the PIPD nanofibers, positively charged PDDA was introduced onto the surface of PIPD nanofibers by using grafting technology. Briefly, the PIPD nanofibers were chemically bonded with 2-bromopropionyl bromide followed by free radical polymerization of PDDA. The PIPD nanofibers grafted with 2-bromopropionyl bromide (PIPD-Br) in the first step were used to initiate the polymerization of PDDA on the surface of PIPD-Br nanofibers.[40] The bromoester groups formed from the reaction of hydroxyl groups on the surface of the PIPD backbone and 2-bromo-propionyl bromide were known as efficient initiators of atom transfer radical polymerization (ATRP) of PDDA.[41] PIPD-g-PDDA copolymers with different PDDA contents were synthesized by controlling the reaction time. The obtained copolymers were denoted as PIPD-g-PDDA1, PIPD-g-PDDA2, PIPD-g-PDDA3, PIPD-g-PDDA4 and PIPD-g-PDDA5, corresponding to the reaction time of 1, 1.5, 2, 4 and 6 h. According to the structural analysis of the products (Fig. S2, ESI†), the PIPD-g-PDDA nanofibers were successfully fabricated, and the PDDA mass fractions were calculated to be 1.2, 5.1, 9.2, 13.8 and 15.3 wt%, respectively. Meanwhile, the zeta potential reached a stable value in a reaction time of 6 h, indicating that the grafting of PDDA had reached a maximum value. Thus PIPD-g-PDDA5 nanofibers were chosen as the skeleton and made into porous
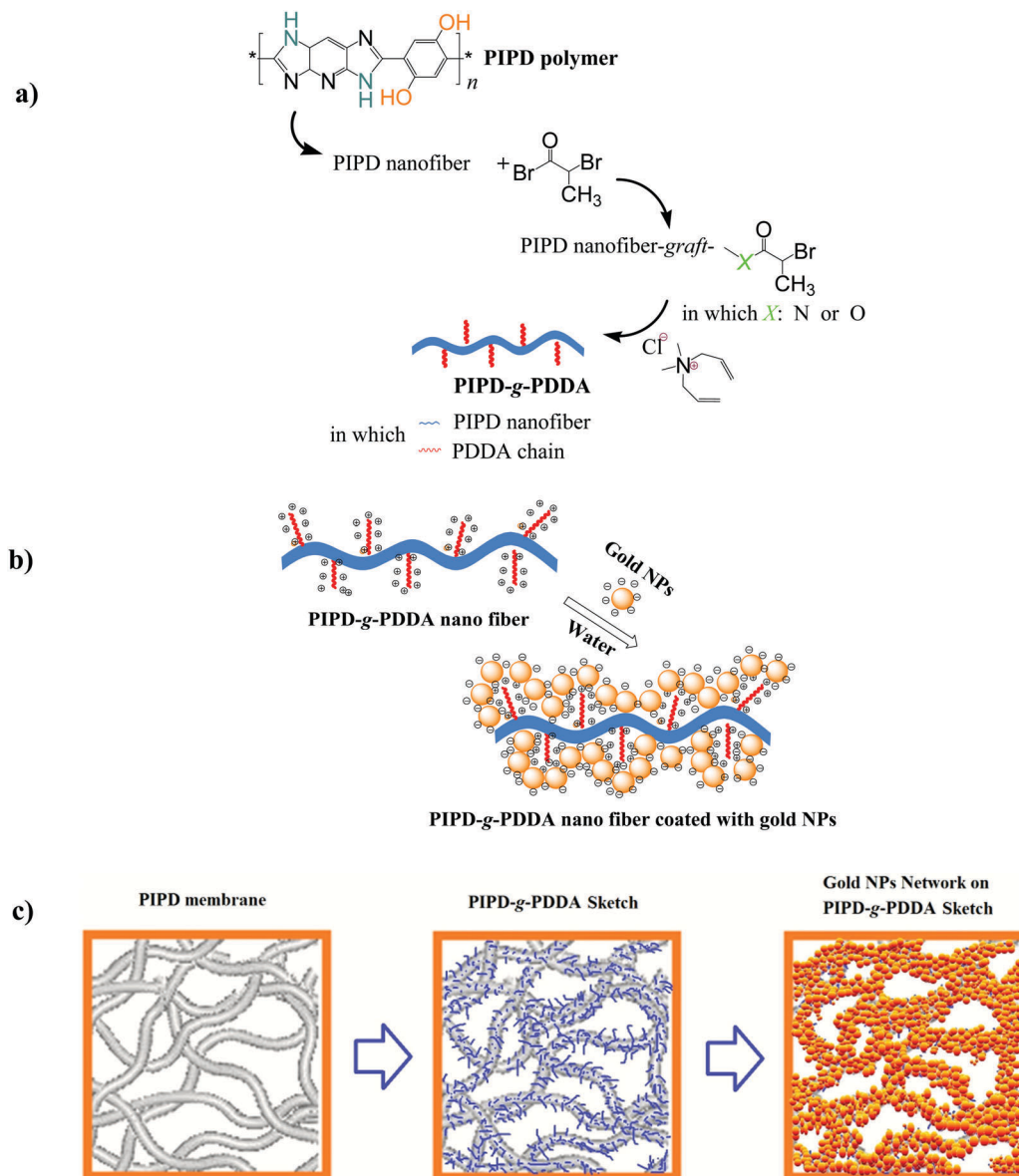
Scheme 1 (a) Synthesis of PIPD-*g*-PDDA, (b) assembly of negatively charged gold NPs on the positively charged surface of PIPD-*g*-PDDA nanofibers, and (c) formation of porous gold composites.

membranes by filtration of their aqueous solution (0.5 mg mL^{-1}) and the thickness was determined by SEM (Fig. S3, ESI†).

The membranes were further washed with DI water thoroughly to remove the residual PDDA monomers that were absorbed on the nanofibers. Finally, aqueous solution of gold nanoparticles (0.428 mg mL^{-1}) with an average size of 9.7 nm and a zeta potential of ~ -48 mV (Fig. S4, ESI†) was filtered through the PIPD-*g*-PDDA5 membrane repeatedly until the degree of gold self-assembly reached saturation conditions. The obtained soft and porous membranes were denoted as PIPD-*g*-PDDA/Au1, PIPD-*g*-PDDA/Au2, PIPD-*g*-PDDA/Au3, PIPD-*g*-PDDA/Au4, PIPD-*g*-PDDA/Au5 and PIPD-*g*-PDDA/Au6. The corresponding gold volume fractions were calculated to be 1.3, 4.1, 9.5, 14.2, 23.9 and 40.5 v%, respectively. Here, the gold volume fraction was defined as $V_{gold}/(V_{gold} + V_{PIPD-g-PDDA})$, in which V_{gold} represents

the volume of gold nanoparticles and $V_{PIPD-g-PDDA}$ is the volume of the PIPD-*g*-PDDA skeleton. The gold volume contents were determined by TGA.

2.2 Characterization

The morphologies and gold distributions of the membranes were observed using a SEM (S-4800, Hitachi Instrument, Inc. Japan) equipped with an Energy Dispersive Spectrometer (EDS). All the PIPD-*g*-PDDA/Au samples were investigated without gold plating. A voltage of 10 kV and a current of 0.54 nA were chosen. The morphology and size of gold NPs were examined using a JEOL JEM-2010 TEM at an accelerating voltage of 120 kV. The morphology and size of gold aggregates on the surface of PIPD-*g*-PDDA nanofibers were examined using AFM (Solver-P47H, NT-MDT, Russia) in tapping mode.

This journal is © The Royal Society of Chemistry 2017

J. Mater. Chem. C, 2017, 5, 1095–1105 | 1097

The FT-IR spectra of the samples were recorded on an AVATAR 360 ESP FT-IR spectrometer (Nicolet, U.S.A.) equipped with a MKII Golden Gate. ^{1}H NMR spectra of samples were obtained on a JEOL JNM-ECA 300 NMR spectrometer using DMSO-d_6 and D_2O as the solvents. UV-visible light absorption spectra (UV-vis, Beijing Purkinje General Instrument Co., Ltd, China, TU-1901) were used to characterize the UV response PIPD and PIPD-g-PDDA copolymers. The zeta potential of gold NPs and PIPD-g-PDDA copolymers was measured using a Zetasizer 2000 from Malvern Instruments (Southborough, MA, USA).

Thermal stability and compositions of the samples were examined on a TGA 2050 Thermogravimetric Analyzer (TA Instruments Inc., U.S.A.) at a heating rate of 10 °C min^{-1} under an air atmosphere. All samples were dried under vacuum at 80 °C for 24 h prior to TGA measurements.

The X-ray diffraction (XRD) patterns of the samples were recorded on a Rigaku D/Max-2200/PC X-ray diffractometer. The EMI shielding effectiveness was measured in the 250 MHz–1.5 GHz frequency range by using an Agilent E4440A PSA High-Performance Spectrum Analyzer.

Conductivity measurements using two-probe and four-probe methods were collected by using a 34401A Digital Multimeter (Agilent Technologies, 6K Digit). The mean values of at least five measurements for every set of films were calculated. An Agilent vector network analyzer (VNA) was employed to evaluate the EMI shielding characteristics of the PIPD-g-PDDA/Au composites in the frequency range of 0.25–1.5 GHz. The porous samples with diameters of 10 mm and thicknesses of 15–50 μm were placed between two waveguide parts that were connected to separate ports of the VNA. The power of input microwave radiation was controlled to 600 mW m^{-2} and the EMI data were obtained.

3. Results and discussion

Fig. 1a and b shows the images of membranes made of PIPD nanofibers and PIPD-g-PDDA5 nanofibers coated with gold nanoparticles, respectively. The SEM images of PIPD-g-PDDA/Au5 nanofibers and the corresponding energy-dispersive spectroscopy (EDS) elemental mapping are displayed in Fig. 1c–e. The red color in the EDS map represents the Au$_L$ characteristic radiation. Apparently, the PDDA chains on the PIPD nanofibers successfully facilitated the ionic self-assembly of gold nanoparticles on the PIPD framework. From the atomic force microscopy (AFM) images (Fig. 1f–h), a gold layer formed by the aggregates of gold nanoparticles with a diameter of 20–120 nm was observed. Fig. 2a–c shows the gold network structures of PIPD-g-PDDA/Au2, PIPD-g-PDDA/Au4 and PIPD-g-PDDA/Au6 membranes, respectively. Meanwhile, the XRD patterns in
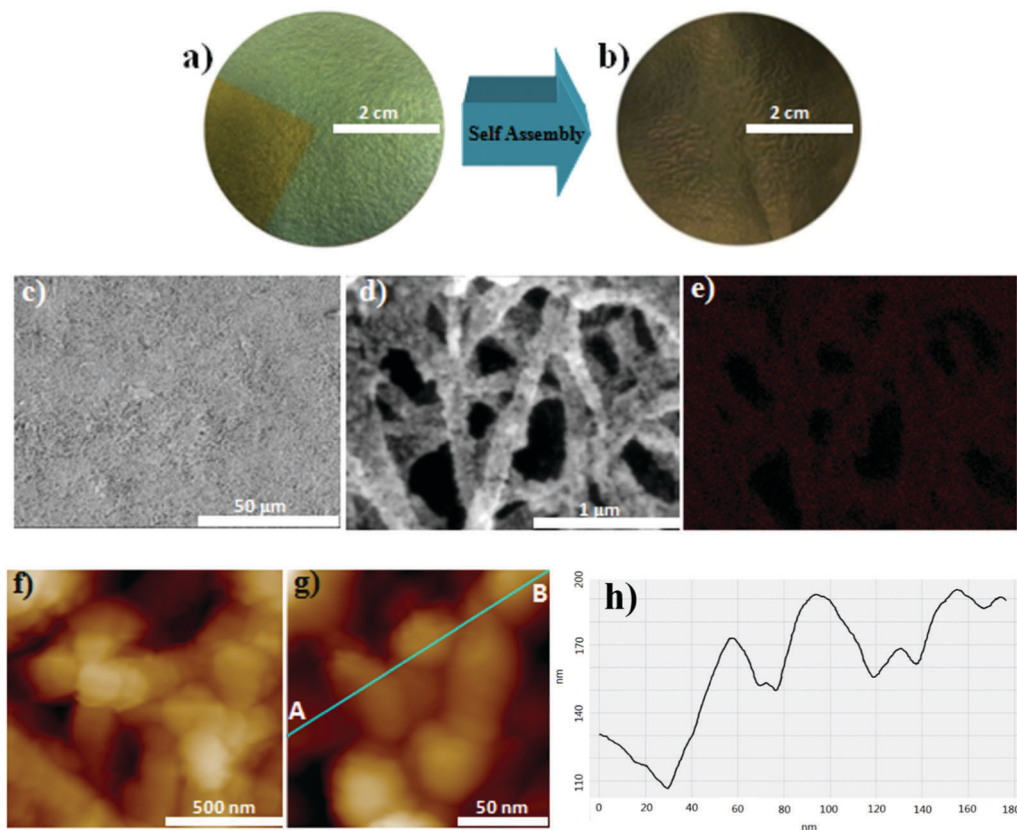

Fig. 1 (a and b) Photography of PIPD and PIPD-g-PDDA/Au5 porous films. The PIPD nanofibers are yellow due to the sputter coated gold for SEM imaging. (c and d) SEM of PIPD-g-PDDA/Au with different magnifications. (e) The corresponding EDS mapping of (d). (f and g) AFM images of the gold layer located on PIPD-g-PDDA/Au5 composites at different magnifications. (h) Corresponding height profile of the trace between A and B shown in (g).
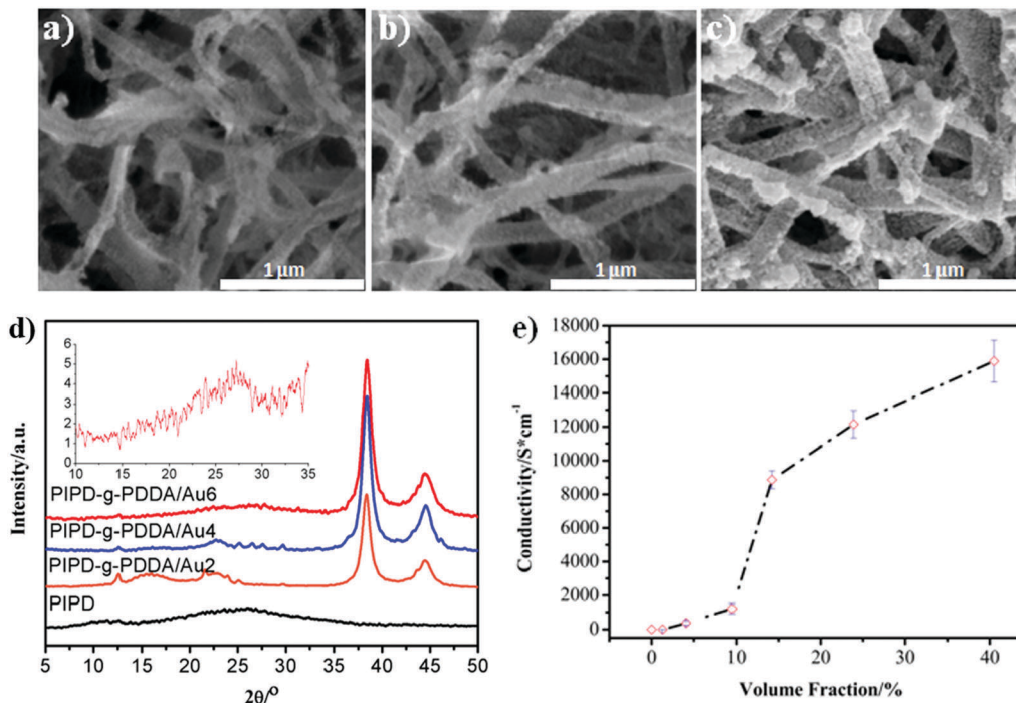
Fig. 2 (a–c) SEM images of PIPD-*g*-PDDA/Au2, PIPD-*g*-PDDA/Au4 and PIPD-*g*-PDDA/Au6 composites, respectively; (d) XRD patterns of PIPD and PIPD-*g*-PDDA/Au films, the inset is the enlarged part of PIPD-*g*-PDDA/Au6; and (e) conductivity of the film *versus* gold contents.

Fig. 2d were used to confirm the presence of both PIPD and gold crystals in those porous films. The diffraction peaks at around $2\theta = 11.9°$ and $25.8°$ of the PIPD nanofibers correspond to the (200) and (100) reflections of the PIPD crystal unit cell in the nanoscale domains.[42–44] Meanwhile, the diffraction peaks at around $2\theta = 38.4°$ and $44.5°$ were assigned to the (111) and (200) reflections of the gold crystal unit cell, respectively.[45,46]

The highly porous nature leads to an ultralow density (0.26 g cm^{-3}) in the as-obtained PIPD-*g*-PDDA/Au network, about 10 times lighter than the solid polymer composites. Despite its ultra-light weight, the porous membrane is highly conductive due to the interconnected 3D gold network, providing a fast electron transport channel within the PIPD-*g*-PDDA/Au network. The electrical conductivity (σ) of all the porous PIPD-*g*-PDDA/Au membranes was tested. σ is observed to increase with increasing the gold content, Fig. 2e, indicating that the σ of the network increased due to the construction of a thicker gold layer. However, the thickness of gold nanoparticles on the PIPD-*g*-PDDA nanofibers should be carefully chosen because thin deposition gives smaller crystal grains and more defects or voids,[47] while thick deposition makes a perfect gold network but reduces the surface area of the gold nanoparticles. Interestingly, the σ of the porous membrane with a gold content of 40.5 v% reached $15\,890 \pm 742$ S cm^{-1}, which is ∼4 orders of magnitude higher than the conventional polymer nanocomposites.[48–50] To the best of our knowledge, it is the highest σ value of polymer composites reported in the related ref. 51. The high σ is attributed to the continuous charge transport pathway given by the connective gold network formed on the nanofibers. Similar conductive network structures have been reported in previous work,[52–55] but they showed much lower σ owing to the severe structural defects and/or high inter-sheet junction contact resistance. Generally, the junction resistance can be significantly reduced using post-treatment methods such as thermal annealing, wet chemical coating, nano-plasmonic welding, and electroweld ing.[56–60] For the gold network formed on the PIPD-*g*-PDDA nanofibers, there are no structural defects and high junction contact resistance observed. As discussed above, the chemically bonded PDDA chains on the surface of PIPD-*g*-PDDA nanofibers made them positively charged in water. Once the negatively charged gold nanoparticles were added, they would absorb on the PIPD-*g*-PDDA nanofibers through strong ionic bonding. The voids of the junction area and other areas of PIPD-*g*-PDDA nanofibers were occupied by the introduced gold nanoparticles gradually. Theoretically, the PDDA chains could be distributed equally on the surface of PIPD nanofibers. Therefore, once there was a void site of gold on the surface of PIPD-*g*-PDDA nanofibers, a group of free PDDA chains or segments would adsorb a group of free gold nanoparticles to fill in this area. Finally, gold networks with good connection were created.

Nevertheless, the PIPD-*g*-PDDA/Au film cannot reach the theoretical σ of a gold layer with a thickness of more than 30 nm at room temperature due to the contact resistance caused by the ligand layer on the gold nanoparticles, which was confirmed by the following heat treatment. The enhanced σ of the PIPD-*g*-PDDA/Au6 was observed to be $18\,300 \pm 1008$ S cm^{-1} when the film was treated at 300 °C for 20 min under a nitrogen atmosphere. The enhanced σ was attributed to the removal of ligands on the gold nanoparticles followed by the increasing

This journal is © The Royal Society of Chemistry 2017

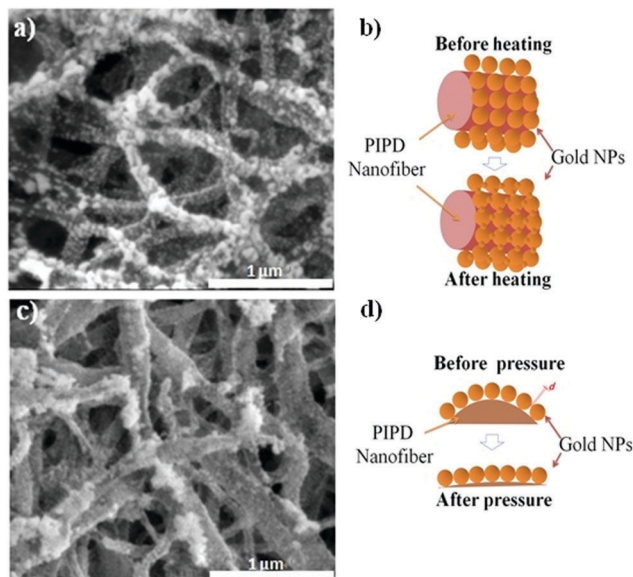*J. Mater. Chem. C*, 2017, 5, 1095–1105 | 1099

Fig. 3   (a) SEM images of the PIPD-g-PDDA/Au6 composites after heating at 300 °C for 20 min; (b) scheme of the gold network changes during the heating process. Gold nanoparticles were fused together when the absorbed ligands were degraded and removed; (c) SEM images of the PIPD-g-PDDA/Au6 composites after pressing (F) at 3 MPa for 2 h; (d) scheme of the gold network changes during the pressing process. Gold nanoparticles are arranged tighter after geometrical deformation of the nanofibers.

gold connection and gold fusion. When the gold content was less than 14.2 v%, the σ of the porous composites was observed to decrease after heat-treatment. The lower the gold content, the faster the decrease in conductivity. For the PIPD-g-PDDA/Au film with a high gold content, taking PIPD-g-PDDA/Au6 for example, the weight of the membrane was decreased by ~0.8% after incubation, and the surface morphology of the film was changed, Fig. 3a. The gold nanoparticles were observed to be fused together and a consolidated gold network was formed, Fig. 3b and Fig. S6 (ESI†). The loss of ligand upon heating has been previously documented for planar gold surfaces and gold nanoparticles.[61–63] The interactions between the polymer, ligands and the gold surface are complex, and their relative individual contribution to gold nanoparticle network is difficult to determine precisely. However, the substantial decrease in the number of charges per nanoparticle (as inferred from the loss of ligands) is responsible for the bridging joints of nanoparticles. Furthermore, the loss of ligands may enhance the polymer PDDA–gold interactions because the amine salt groups of PDDA may chemisorb on a more exposed gold surface,[64a] thereby preventing the macrophase separation of the nanoparticles from the block copolymer. Meanwhile, the loss of ligands from the nanoparticles increased the volume fraction of gold in the nanoparticles and thus improved the ability of the membrane to survive the pyrolysis.

In addition to the heat treatment, compression is another effective way to improve the σ of the membrane. The σ of the PIPD-g-PDDA/Au6 film was increased to $22\,240 \pm 998$ S cm^{-1} under a pressure of 3 MPa for 2 h. Fig. 3c and Fig. S5 (ESI†)

show the morphology of composites. Under the compression treatment, the σ of the membrane was improved in two main ways. On one hand, the gold nanoparticles were arranged more tightly due to the intersecting structure changes of the PIPD-g-PDDA nanofibers from circle to oblate, which lowered the contact resistance of the gold network (Fig. 3d). On the other hand, the decrease of the film thickness by 16.3% also facilitated the increase of σ, expressed as $\sigma = 1/(R_f \times t)$,[65] where R_f is the four-electrode resistivity and t is the thickness of the films.

The thermal stability of PIPD-g-PDDA/Au nanofibers with different gold contents was also studied, Fig. 4a. All the curves show two-step degradation. The first one at about 224–312 °C and the second one at about 475–550 °C, Fig. 4b, are attributed to the degradation of organic PDDA chains and PIPD chains. Obviously, the nanocomposites show a much lower initial degradation temperature than the PIPD fibers, which is caused by the unstable PDDA chains in the composites. Also, the PIPD nanofibers showed a weaker thermal stability than PIPD fibers because of the decreased size and significantly increased –OH, –NH$_2$ and –COOH groups on the surface. However, the stabilities of PDDA and PIPD nanofibers were improved by gold
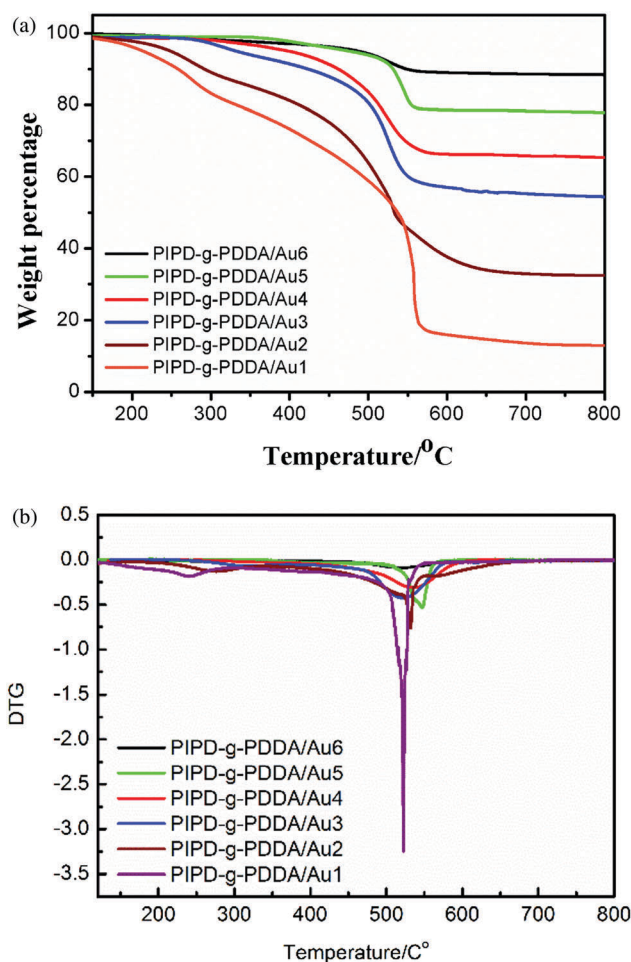

Fig. 4   (a) TGA curves and (b) of PIPD-g-PDDA/Au with different gold contents (in air).
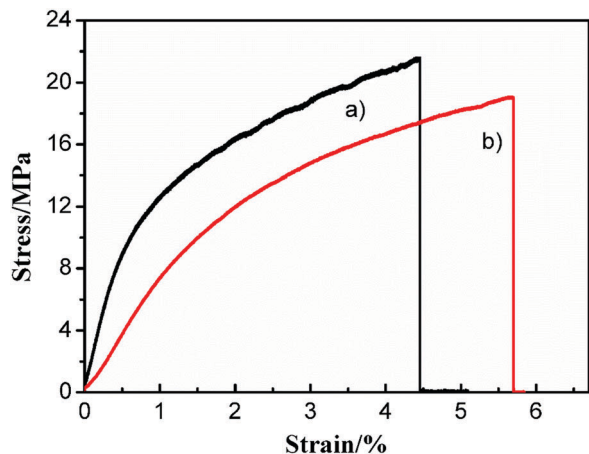
Fig. 5 Mechanical properties of (a) PIPD-*g*-PDDA5/Au and (b) PIPD-*g*-PDDA5.

Fig. 6 Film conductivity change after different bending cycles. The bending radius is 1 cm.

nanoparticle coating. The gold nanoparticle coating formed a thermal protection layer on the PDDA chains and PIPD skeletons and the gold with good thermal conductivity favored the transfer of heat to the surrounding when the composites were heated.

The effect of gold on the mechanical properties of the membrane was investigated, Fig. 5. Owing to the weak interactions between the PIPD-*g*-PDDA nanofibers, the membrane shows a tensile strength of 19.3 MPa and an elongation at break of 5.68%. After the loading of the gold nanoparticles, the tensile strength was increased to 21.7 MPa because of the gold coating on the surface of the skeleton, which is similar to the enhanced tensile strength observed in the carbon nanotube adsorbed polyamide nanofibers.[64b] Meanwhile, the elongation at break was decreased to 4.43%. These membranes are observed to exhibit a behavior of plastic deformation. The addition of gold nanoparticles in the polymer increased the tensile strength by 12.4% as compared with the pure polymer membranes.

The mechanical flexibility is another advantage of these polymer-based gold composites. As shown in Fig. S7 (ESI†), The cyclic bending test up to 1000 cycles was conducted for the PIPD-*g*-PDDA/Au composites to quantitatively investigate their flexibility and durability. It can be seen that the σ of the PIPD-*g*-PDDA/Au composites with different Au loadings was maintained after bending, Fig. 6. Taking PIPD-*g*-PDDA/Au6 (the most rigid membrane in PIPD-*g*-PDDA/Au1–6 because of its highest gold content) as an example, superior bending durability was observed while the σ was decreased only by ~7.8% after the whole 1000 bending test. Three main reasons are responsible for the high flexibility of the gold network. Firstly, the freezing point of the PDDA layer that adhered both PIPD nanofibers and gold nanoparticles is only −2.8 °C. These PDDA layers behave as fluid at room temperature and work as plasticizers for the gold network.[66,67a] The PDDA layer deforms easily according to the force and thus absorbs part of the bending energies, aiding the maintenance of the connective gold network. Secondly, the gold nanoparticles adsorbed on the PDDA coils are ductile because the adhesion interaction by
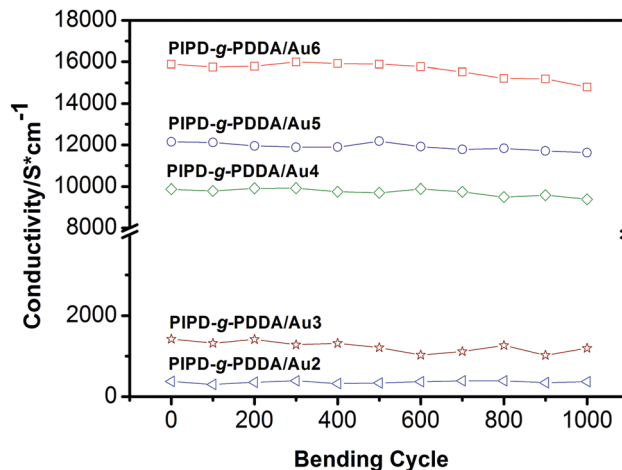
sodium citrate among gold nanoparticles is not strong. The formed gold network can be destroyed and reconstructed during the bending, similar to the carbon nanotubes and graphene reinforced polyurethane nanocomposites.[67b] Finally, the porous PIPD nanofiber structures can absorb most of the deforming energy and withstand a larger degree of deformation.[47]

The electromagnetic properties of PIPD-*g*-PDDA/Au composites were determined by complex permittivity ($\varepsilon = \varepsilon' - i\varepsilon''$) and permeability ($\mu = \mu' - i\mu''$).[68] The microwave properties of PIPD-*g*-PDDA/Au composites are mainly due to the reflection effort. In addition, the 3-D structure of the gold network as well as the large surface area of the PIPD-*g*-PDDA/Au composites promotes multiple reflections of the incident microwaves inside the composites. However, due to the absence of the magnetic component, only relative complex permittivity is available, while the relative complex permeability is $\mu = \mu' + \mu'' = 1' + 0''$. The real part of the EM parameters (ε') is a measure of the amount of polarization taking place in the material and represents the capability for electric storage, while the imaginary part (ε'') represents the energy loss ability. Fig. 7a shows the real parts of the complex permittivity of the PIPD composites. As is shown, ε' decreases with the increase of frequency, showing a frequency-dependent dielectric response. For instance, the ε' value of PIPD-*g*-PDDA/Au3 reaches 8.12 at 250 MHz, and the ε' of PIPD-*g*-PDDA/Au6 shows the maximum of 9.07 at the same frequency. This behaviour is caused by the lag of the induced electric field reversed external electric field at high frequency.[69] Fig. 7b shows the imaginary parts of the complex permittivity of the composites. Similarly, the ε'' values improve significantly with increasing the gold content. Higher permittivity leads to higher dielectric loss due to the presence of a conductive gold network.

The EMI shielding effectiveness (SE_T) of the composites is defined as the logarithmic ratio of P_i to outgoing power P_o of radiation, including the reflection from the material surface (SE_R), the absorption of electromagnetic energy (SE_A), and the multiple internal reflection of electromagnetic radiation (SE_M).
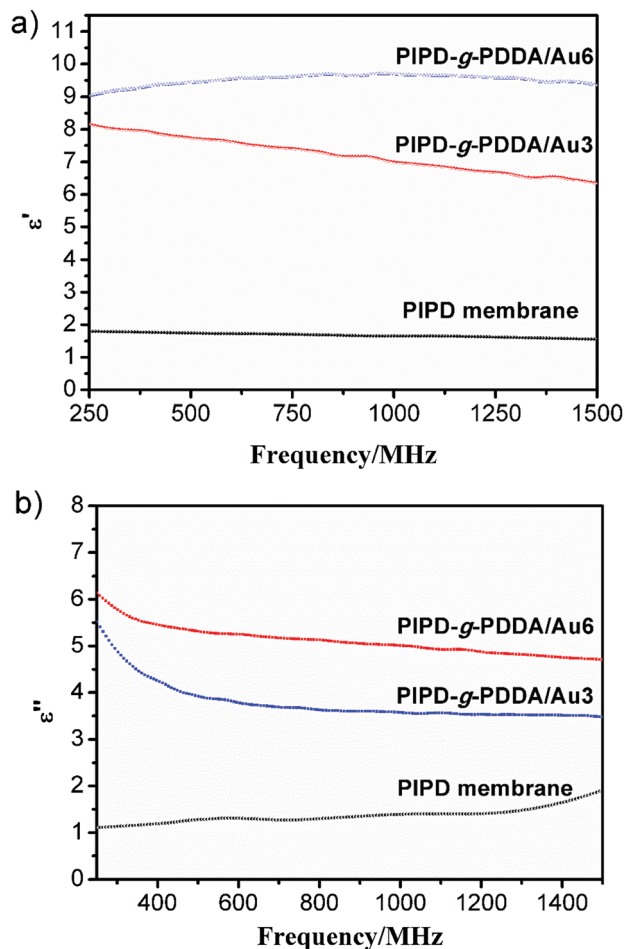
Fig. 7 (a) Real part and (b) imaginary part of complex permittivity of the porous PIPD membrane and PIPD-*g*-PDDA/Au composites of the EM parameters.

When $SE_A > 10$ dB, SE_M can be neglected. Hence, the EMI SE of the material can be expressed as follows:[68]

$$SE_T = 10 \log(P_i/P_o) = SE_A + SE_R \qquad (1)$$

$$SE_A = 8.686d\sqrt{\pi f \sigma \mu} \qquad (2)$$

$$SE_R = 20 \log\left(\frac{\sqrt{\mu_0 \sigma}}{4\sqrt{2\pi f \mu \varepsilon_0}}\right) \qquad (3)$$

where d is the average thickness of the composite films, f is the frequency of the electromagnetic waves, σ is the electrical conductivity of the materials, μ is the magnetic permeability of the materials with a relationship of $\mu = \mu_0 \mu_r$ ($\mu_0 = 4\pi \times 10^{-7}$ H m^{-1}, $\mu_r = 1$ in this case), $\varepsilon_0 = 8.854 \times 10^{-12}$ F m^{-1}.

These highly conductive flexible composites demonstrated high EMI shielding performance, Fig. 8a and Fig. S8 (ESI†). The EMI shielding effectiveness of the PIPD-*g*-PDDA/Au6 is measured to be −64.9 dB over 0.25–1.5 GHz. The PIPD-*g*-PDDA/Au3 composites with a smaller σ show an EMI shielding effectiveness of −33.7 dB over 0.25–1.5 GHz. It is worth noting that PIPD-*g*-PDDA/Au composites are more than 50 times thinner
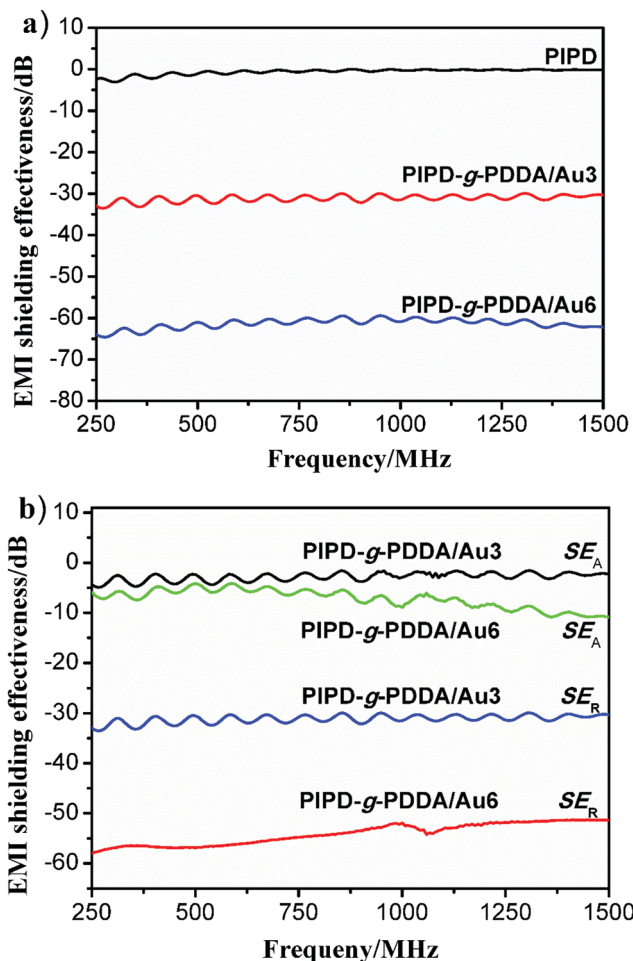

Fig. 8 (a) Total EMI shielding effectiveness, and (b) SEA and SER of the PIPD-*g*-PDDA/Au network with different gold contents measured in the frequency range of 0.25–1.5 GHz.

than the composites reported in the previous study (as shown in Table 1) while exhibiting a higher shielding effectiveness. Importantly, the gold networks showed a lower equivalent gold thickness than the skin depth of bulk gold in this frequency range. For example, if all the gold was extracted from the PIPD-*g*-PDDA/Au3 composites and made into gold wafer of the same radius, the thickness of the wafer will be as small as 0.13 μm. This value is 50 times smaller than the skin depth of the gold film (δ) at this frequency calculated by $\delta = 1/\text{sqrt}(\pi \cdot \mu \cdot f \cdot \sigma)$ (where f is the frequency, σ the electrical conductivity, and μ the magnetic permeability of the materials),[14] indicating that the PIPD-*g*-PDDA/Au composites are much more effective than the gold film for EMI shielding.

To shed light on the EMI shielding mechanism of the PIPD-*g*-PDDA/Au composites, Fig. 8b shows SE_A and SE_R in the range of 0.25–1.5 GHz. The contribution of SE_R to SE_T is observed to be much larger than that of SE_A. These results suggest that the PIPD-*g*-PDDA/Au composites are both reflective and absorptive to electromagnetic radiation in this frequency range, and the reflection is the dominant shielding mechanism. Scheme 2 depicts the electromagnetic wave transfer across

Table 1 EMI shielding effectiveness of different materials

Materials	Thickness (mm)	Electrical conductivity (S cm^{-1})	Shielding performance (dB)	Ref.
MWCNT/PCL foam	20.00	—	60.0	2
CNT/polystyrene	4.00		30.0	7
Aluminium flakes/PES	2.90	—	39.0	1
Graphene/PMMA	2.40	8	25.0	24
SWCNT/epoxy	1.50	—	20.0	63
Graphene/PDMS foam	1.00	2	30.0	9
CNF–GN networks	0.27	8	28.0	64
PIPD-*g*-PDDA/Au	**0.02**	**15 890**	**66.9**	This work
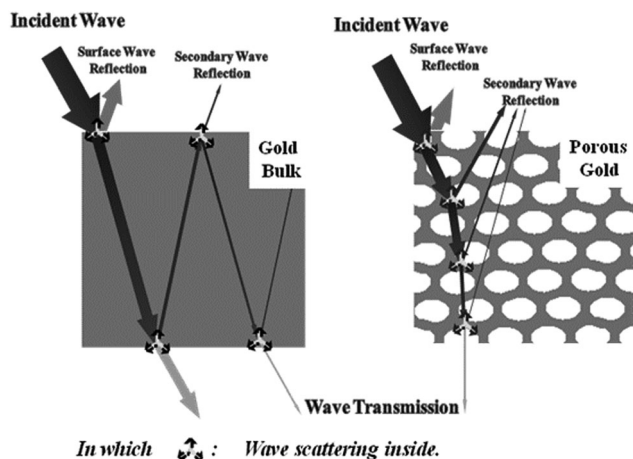
Scheme 2 Electromagnetic wave transfer in (a) gold bulk and (b) porous PIPD-*g*-PDDA/Au composites.

the PIPD-*g*-PDDA/Au composites. Similar to the EMI shielding mechanism of the carbon nanofibers, multi-wall and single-walled CNT/polymer composites,[8,23] where the reflection is the major contribution of the EMI shielding. The 3-D structure of the gold network, as well as the large surface area of the PIPD-*g*-PDDA/Au composites, promote multiple reflections of the incident microwaves inside the composites and consequently are responsible for the reflective-dominant EMI shielding. To further improve the EMI shielding effectiveness of the composites, multiple membranes were stacked together. As expected, the stacked membrane showed a much better EMI shielding effectiveness than one single membrane. More than 93 dB shielding effectiveness in the X-band frequency range was achieved by stacking 4 layers of PIPD-*g*-PDDA/Au6 membranes together when the total thickness was about 0.1 mm.

4. Conclusion

Ionic self-assembly was used to prepare conductive gold composites with PIPD-*g*-PDDA nanofibers as the templates. The formed junction-free gold networks greatly enhanced the conductivity of the membrane, as well as the big gold active surface. The porous PIPD-*g*-PDDA/Au composites demonstrated extremely lightweight and outstanding EMI shielding effectiveness and mechanical flexibility. Meanwhile, these porous composites had a density of <0.26 g cm^{-3} and showed excellent softness.

No obvious conductivity degradation was observed even after repeatedly bending to a radius of 1 cm for 1000 times. The shielding effectiveness of those membranes reached 64.9 dB in the 0.25–1.5 GHz frequency range when the thickness of the membrane was only 20 μm, which far surpassed the best values of the metals and carbon-based composite materials. The excellent flexibility of these composites also gave it a stable EMI shielding performance under mechanical deformation. The good flexibility, high conductivity and excellent EMI shielding performance enable the potential use of this thin lightweight PIPD-*g*-PDDA/Au membrane as high-performance EMI shielding materials in next-generation flexible electronics, such as soft portable electronic products, roll-up displays, wearable devices, and conformable health-monitoring electronic skins.[70,71]

Acknowledgements

Notes and references

1 J. Zhu, S. Wei, N. Haldolaarachchige, D. P. Young and Z. Guo, *J. Phys. Chem. C*, 2011, **115**, 15304–15310.

2 P. Saini, M. Arora, G. Gupta, B. K. Gupta, V. N. Singh and V. Choudhary, *Nanoscale*, 2013, **5**, 4330–4336.

3 W. Xia, C. Jin, S. Kundu and M. Muhler, *Carbon*, 2009, **47**, 919–922.

4 Z. Guo, S. Park, H. T. Hahn, S. Wei, M. Moldovan, A. B. Karki and D. P. Young, *J. Appl. Phys.*, 2007, **10**, 09M511.

5 H.-D. Huang, C.-Y. Liu, D. Zhou, X. Jiang, G.-J. Zhong, D.-X. Yan and Z.-M. Li, *J. Mater. Chem. A*, 2015, **3**, 4983–4991.

6 Q. He, T. Yuan, X. Zhang, X. Yan, J. Guo, D. Ding, M. A. Khan, D. P. Young, A. Khasanov, Z. Luo, J. Liu, T. Shen, X. Liu, S. Wei and Z. Guo, *J. Phys. Chem. C*, 2014, **118**, 24784–24796.

7 H. Wang, L. Wu, J. Jiao, J. Zhou, Y. Xu, H. Zhang, Z. Jiang, B. Shen and Z. Wang, *J. Mater. Chem. A*, 2015, **3**, 6517–6525.

8 Y. Yang, M. C. Gupta, K. L. Dudley and R. W. Lawrence, *Nano Lett.*, 2005, **5**, 2131–2134.

9 M. H. Al-Saleh, G. A. Gelves and U. Sundararaj, *Composites, Part A*, 2011, **42**, 92–97.

10 M. Chen, L. Zhang, S. Duan, S. Jing, H. Jiang, M. Luo and C. Li, *Nanoscale*, 2014, **6**, 3796–3803.

11 Z. Chen, C. Xu, C. Ma, W. Ren and H.-M. Cheng, *Adv. Mater.*, 2013, **25**, 1296–1300.

12 G. A. Gelves, B. Lin, U. Sundararaj and J. A. Haber, *Adv. Funct. Mater.*, 2006, **16**, 2423–2430.

13 L. Li and D. Chung, *Polym. Compos.*, 1993, **14**, 467–472.

14 W.-L. Song, M.-S. Cao, M.-M. Lu, S. Bi, C.-Y. Wang, J. Liu, J. Yuan and L.-Z. Fan, *Carbon*, 2014, **66**, 67–76.

15 Z. Wang, L. Wu, F. Wang, Z. Jiang and B. Shen, *J. Mater. Chem. A*, 2013, **1**, 9746–9751.

16 D. Micheli, R. B. Morles, M. Marchetti, F. Moglie and V. M. Primiani, *Carbon*, 2014, **68**, 149–158.

17 F. Moglie, D. Micheli, S. Laurenzi, M. Marchetti and V. M. Primiani, *Carbon*, 2012, **50**, 1972–1980.

18 M. Mahmoodi, M. Arjmand, U. Sundararaj and S. Park, *Carbon*, 2012, **50**, 1455–1464.

19 D.-X. Yan, P.-G. Ren, H. Pang, Q. Fu, M.-B. Yang and Z.-M. Li, *J. Mater. Chem.*, 2012, **22**, 18772–18774.

20 H. Kim, K. Kim, S. Lee, J. Joo, H. Yoon, S. Cho, S. Lyu and C. Lee, *Curr. Appl. Phys.*, 2004, **4**, 577–580.

21 K. Oh, S. M. Hong and Y. Seo, *Polym. Adv. Technol.*, 2014, **25**, 1366–1370.

22 H. Wei, D. Ding, S. Wei and Z. Guo, *J. Mater. Chem. A*, 2013, **1**, 10805–10813.

23 Y. Yang, M. C. Gupta, K. L. Dudley and R. W. Lawrence, *Adv. Mater.*, 2005, **17**, 1999–2003.

24 M. H. Al-Saleh and U. Sundararaj, *Carbon*, 2009, **47**, 1738–1746.

25 P. Saini and M. Arora, *J. Mater. Chem. A*, 2013, **1**, 8926–8934.

26 Z. Chen, W. Ren, L. Gao, B. Liu, S. Pei and H.-M. Cheng, *Nat. Mater.*, 2011, **10**, 424–428.

27 H.-B. Zhang, Q. Yan, W.-G. Zheng, Z. He and Z.-Z. Yu, *ACS Appl. Mater. Interfaces*, 2011, **3**, 918–924.

28 H. Qi, J. Liu, S. Gao and E. Mader, *J. Mater. Chem. A*, 2013, **1**, 2161–2168.

29 W.-L. Song, L.-Z. Fan, M.-S. Cao, M.-M. Lu, C.-Y. Wang, J. Wang, T.-T. Chen, Y. Li, Z.-L. Hou and J. Liu, *J. Mater. Chem. C*, 2014, **2**, 5057–5064.

30 S. Wen and D. Chung, *Cem. Concr. Res.*, 2004, **34**, 329–332.

31 D. V. Kosynkin, A. L. Higginbotham, A. Sinitskii, J. R. Lomeda, A. Dimiev, B. K. Price and J. M. Tour, *Nature*, 2009, **458**, 872–876.

32 Y. Takahashi, T. Kumano and S. Nishikawa, *Macromolecules*, 2004, **37**, 6827–6832.

33 M. B. Vázquez-Santos, M. Amelia, J. Tascón, J. Rouzaud, E. Geissler and K. László, *Carbon*, 2011, **49**, 2960–2970.

34 J. Fan, J. Wang, Z. Shi, S. Yu and J. Yin, *Mater. Chem. Phys.*, 2013, **141**, 861–868.

35 S. Ifuku, H. Maeta, H. Izawa, M. Morimoto and H. Saimoto, *RSC Adv.*, 2014, **4**, 40377–40380.

36 J. Zhu, W. Cao, M. Yue, Y. Hou, J. Han and M. Yang, *ACS Nano*, 2015, **9**, 2489–2501.

37 E. Nagy, *Basic equations of the mass transport through a membrane layer*, Elsevier, 2012.

38 L. Sun and R. M. Crooks, *J. Am. Chem. Soc.*, 2000, **122**, 12340–12345.

39 H. Verweij, M. C. Schillo and J. Li, *Small*, 2007, **3**, 1996–2004.

40 Y. Liu, V. Klep, B. Zdyrko and I. Luzinov, *Langmuir*, 2004, **20**, 6710–6718.

41 W. A. Braunecker and K. Matyjaszewski, *Prog. Polym. Sci.*, 2007, **32**, 93–146.

42 A. Andres Leal, J. M. Deitzel and J. W. Gillespie Jr, *Compos. Sci. Technol.*, 2007, **67**, 2786–2794.

43 Y. Takahashi, *Macromolecules*, 2002, **35**, 3942–3945.

44 K. Yu, Z. Du, H. Li and C. Zhang, *Polym. Eng. Sci.*, 2010, **50**, 396–401.

45 J. Hu, Z. Wang and J. Li, *Sensors*, 2007, **7**, 3299–3311.

46 S. V. Selvaganesh, J. Mathiyarasu, K. Phani and V. Yegnaraman, *Nanoscale Res. Lett.*, 2007, **2**, 546–549.

47 P.-C. Hsu, D. Kong, S. Wang, H. Wang, A. J. Welch, H. Wu and Y. Cui, *J. Am. Chem. Soc.*, 2014, **136**, 10593–10596.

48 X. Zhang, X. Yan, Q. He, H. Wei, J. Long, J. Guo, H. Gu, J. Yu, J. Liu, D. Ding, L. Sun, S. Wei and Z. Guo, *ACS Appl. Mater. Interfaces*, 2015, **7**, 6125–6138.

49 J. Guo, X. Zhang, H. Gu, Y. Wang, X. Yan, D. Ding, J. Long, S. Tadakamalla, Q. Wang, M. A. Khan, J. Liu, X. Zhang, B. L. Weeks, L. Sun, D. P. Young, S. Wei and Z. Guo, *RSC Adv.*, 2014, **4**, 36560–36572.

50 X. Zhang, O. Alloul, J. Zhu, Q. He, Z. Luo, H. A. Colorado, N. Haldolaarachchige, D. P. Young, T. D. Shen, S. Wei and Z. Guo, *RSC Adv.*, 2013, **3**, 9453–9464.

51 Y. Kim, J. Zhu, B. Yeom, M. Di Prima, X. Su, J.-G. Kim, S. J. Yoo, C. Uher and N. A. Kotov, *Nature*, 2013, **500**, 59–63.

52 Y. Xia and J. Ouyang, *J. Mater. Chem.*, 2011, **21**, 4927–4936.

53 D. Alemu, H.-Y. Wei, K.-C. Ho and C.-W. Chu, *Energy Environ. Sci.*, 2012, **5**, 9662–9671.

54 S. Soltanian, R. Rahmanian, B. Gholamkhass, N. M. Kiasari, F. Ko and P. Servati, *Adv. Energy Mater.*, 2013, **3**, 1332–1337.

55 P.-C. Hsu, H. Wu, T. J. Carney, M. T. McDowell, Y. Yang, E. C. Garnett, M. Li, L. Hu and Y. Cui, *ACS Nano*, 2012, **6**, 5150–5156.

56 P.-C. Hsu, S. Wang, H. Wu, V. K. Narasimhan, D. Kong, H. R. Lee and Y. Cui, *Nat. Commun.*, 2013, **4**, 1–7.

57 L. Hu, H. S. Kim, J.-Y. Lee, P. Peumans and Y. Cui, *ACS Nano*, 2010, **4**, 2955–2963.

58 E. C. Garnett, W. Cai, J. J. Cha, F. Mahmood, S. T. Connor, M. G. Christoforo, Y. Cui, M. D. McGehee and M. L. Brongersma, *Nat. Mater.*, 2012, **11**, 241–249.

59 T.-B. Song, Y. Chen, C.-H. Chung, Y. Yang, B. Bob, H.-S. Duan, G. Li, K.-N. Tu, Y. Huang and Y. Yang, *ACS Nano*, 2014, **8**, 2804–2811.

60 J. Zhu, Z. Luo, S. Wu, N. Haldolaarachchige, D. P. Young, S. Wei and Z. Guo, *J. Mater. Chem.*, 2012, **22**, 835–844.

61 E. a. a. Delamarche, B. Michel, H. Kang and C. Gerber, *Langmuir*, 1994, **10**, 4103–4108.

1104 | *J. Mater. Chem. C*, 2017, **5**, 1095–1105

This journal is © The Royal Society of Chemistry 2017

62 S. C. Warren, L. C. Messina, L. S. Slaughter, M. Kamperman, Q. Zhou, S. M. Gruner, F. J. DiSalvo and U. Wiesner, *Science*, 2008, **320**, 1748–1752.

63 M. J. Hostetler, A. C. Templeton and R. W. Murray, *Langmuir*, 1999, **15**, 3782–3789.

64 (*a*) B. J. Kim, J. Bang, C. J. Hawker and E. J. Kramer, *Macromolecules*, 2006, **39**, 4108-4114; (*b*) X. Guan, G. Zheng, K. Dai, C. Liu, X. Yan, C. Shen and Z. Guo, *ACS Appl. Mater. Interfaces*, 2016, **8**, 14150–14159.

65 S. Chen, W. Cai, R. D. Piner, J. W. Suk, Y. Wu, Y. Ren, J. Kang and R. S. Ruoff, *Nano Lett.*, 2011, **11**, 3519–3525.

66 M. A. S. A. Samir, A. M. Mateos, F. Alloin, J.-Y. Sanchez and A. Dufresne, *Electrochim. Acta*, 2004, **49**, 4667–4677.

67 (*a*) P. Podsiadlo, S.-Y. Choi, B. Shim, J. Lee, M. Cuddihy and N. A. Kotov, *Biomacromolecules*, 2005, **6**, 2914–2918; (*b*) H. Liu, J. Gao, W. Huang, K. Dai, G. Zheng, C. Liu, C. Shen, J. Guo and Z. Guo, *Nanoscale*, 2016, **8**, 12977–12989.

68 A. P. Singh, P. Garg, F. Alam, K. Singha, R. B. Mathurb, R. P. Tandonc, A. Chandrac and S. K. Dhawan, *Carbon*, 2012, **50**, 3868–3875.

69 J. Liang, Y. Wang, Y. Huang, Y. Ma, Z. Liu, J. Cai, C. Zhang, H. Gao and Y. Chen, *Carbon*, 2009, **47**, 922–925.

70 J. A. Rogers, T. Someya and Y. Huang, *Science*, 2010, **327**, 1603–1607.

71 T. Sekitani, Y. Noguchi, K. Hata, T. Fukushima, T. Aida and T. Someya, *Science*, 2008, **321**, 1468–1472.

This journal is © The Royal Society of Chemistry 2017

J. Mater. Chem. C, 2017, **5**, 1095–1105 | **1105**